Original Paper

Joint inversion of crack properties of tight carbonates from electrical conductivity and ultrasonic velocity

Lin Zhang [a], Li Gao [a], Jing Ba [a, *], José M. Carcione [a, b], Jin-Yi Min [a]

[a] School of Earth Sciences and Engineering, Hohai University, Nanjing, 211000, Jiangsu, China
[b] National Institute of Oceanography and Applied Geophysics — OGS, Borgo Grotta Gigante 42c, Trieste, 34010, Sgonico, Italy

ARTICLE INFO

ABSTRACT

Understanding the effects of cracks on the elastic and electrical properties of tight carbonates is crucial for the exploration and development of deep and ultra-deep carbonate reservoirs. In this work, the porosity, electrical conductivity and ultrasonic velocities of two brine-saturated carbonate samples (where the pore space is dominated by cracks) are measured jointly at different effective pressures (5−90 MPa), as well as the velocities with saturating nitrogen at the same pressure conditions. The results show non-linear changes in the measured values, indicating a correlation with the presence of cracks. To analyze the pressure-dependent elastic and electrical properties, an approach combining a multiphase Kachanov model with a multiphase reformulated electrical differential effective medium (REDEM) model is proposed. This approach agrees well with the pressure-dependent experimental results of brine-saturated carbonate samples. The crack aspect ratio spectra are estimated using the experimental porosity as a constraint to improve the accuracy of the inverted crack geometry. The spectra from the elastic (electrical) inversion are input into the multiphase REDEM (Kachanov) model to predict the electrical conductivity (wave velocities). Comparisons with laboratory measurements show the ability of the proposed approach to estimate elastic wave velocities from the electrical conductivity using the inverted crack geometry, and vice versa.

1. Introduction

With the increasing demand of hydrocarbon energy, carbonate reservoirs, one of the most important oil and gas resources widely distributed worldwide, presents substantial exploitation potential (Guo et al., 2013; Jia, 2020). Currently, the exploration and development of carbonate reservoirs is shifting to deep (4500−6000 m) and ultra-deep (>6000 m) formations. Reservoirs at these depths often undergo multiple diagenetic and alteration processes, characterized by low porosity, low permeability, diverse diagenesis, strong heterogeneity and complex pore geometry. These features significantly increase the challenges in the geophysical characterization of these reservoirs. Therefore, investigating the rock-physics properties of tight carbonates and understanding their correlations with the pore geometry are crucial for the effective geophysical detection of these reservoirs.

The initial focus was primarily on conducting ultrasonic experiments to analyze the relationships between the elastic properties of carbonates and factors such as porosity, temperature and pressure conditions in the reservoir, fluid type, saturation, and clay content (e.g., Anselmetti et al., 1997; Assefa et al., 2003; Ba et al., 2018; Baechle et al., 2005; El-Husseiny and Vanorio, 2015; Liu et al., 2006; Ruan et al., 2023), and pore geometry has been shown to play a central role in controlling variations in elastic rock properties (e.g. Anselmetti and Eberli, 1993; Bakhorji and Schmitt, 2022; Eberli et al., 2003; Kumar and Han, 2005; Sayers, 2008; Teillet et al., 2021; Wei et al., 2021, 2022). Since pore fluid flow within pores can be induced at different scales by acoustic wave excitation, this behavior leads to different response characteristics of elastic waves in different frequency bands (e.g., Ba et al., 2017, 2023; Batzle et al., 2006; Guo and Gurevich, 2020; Zhang et al., 2021). Forced oscillation experiments are also conducted to investigate the seismic properties of carbonates. Adam et al. (2006) measured the elastic moduli of nine carbonate samples in the frequency range (3−3000 Hz, 0.8 MHz), and analyzed the effects of different fluid types on the elastic moduli. Borgomano et al. (2017) investigated the dispersion and attenuation of the elastic moduli in

an oolitic limestone characterized by a bimodal porosity distribution (where the content of intragranular micropores is comparable to that of intergranular macropores) under dry, water- and glycerol-saturated conditions in a range of 0.001–1 Hz and 1 MHz, and showed the absence of squirt flow between the microporous oolites and the macropores. Subsequently, Borgomano et al. (2019) investigated the dispersion and attenuation of carbonate rocks with different microstructures and identified cracked intergranular cement and uncemented grain contacts as the main contributors to the significant squirt-flow dispersion in seismic and logging frequency bands. Zhang et al. (2022a) modeled the effects of different water saturations on the P-wave velocity and attenuation of a limestone at seismic frequencies (2–500 Hz), and analyzed the evolution of gas patches with increasing gas saturation using a wave propagation theory of partially saturated rock with a fractal distribution of patch size.

Similarly, most experimental studies have been conducted to investigate the effects of porosity, pore structure, pore fluid type and mineral composition on the resistivity (reciprocal of electrical conductivity) of carbonates (e.g., Ara et al., 2001; Behin, 2004; Brace et al., 1965; Deng et al., 2000; Li and Shi, 2002; Kim and Manghnani, 1992; Nourani et al., 2023; Regnet et al., 2015). Based on a large number of rock physics experiments, Archie (1942) originally proposed an empirical relationship between conductivity and porosity, i.e., the Archie equation, where the value of the cementation exponent m in the equation is closely related to the pore geometry (e.g., Tariq et al., 2020; Wei et al., 2015; Yue, 2019). The complex pore structure of carbonates can lead to a strong variation of the m value (Borai, 1987; Tian et al., 2019; Towle, 1962; Zhao and Chen, 2015). Tian et al. (2020) selected eight full-diameter carbonate samples and systematically conducted nuclear magnetic resonance (NMR), electricity, porosity and permeability, mercury injection and thin section studies to explore the relationship between pore size and morphology, pore structure complexity and resistivity, and found that a constant m value could not effectively describe the properties of the reservoir. Zhu et al. (2023) proposed a novel approach to characterize the formation factor, which fully considered the influence of different pore structures on the conductivity of pores at different positions in the pore space. The predicted results agreed well with the experimental data for the seven rock types and sediments.

In contrast, there are only a few experimental studies on the elastic and electrical properties of tight carbonate rocks. Pan et al. (2015) analyzed the relationships between ultrasonic velocity and the average specific surface area, average pore radius, pore roundness, and average aspect ratio of carbonates by conducting ultrasonic experiments and thin section testing. Similarly, Li et al. (2020) conducted broadband experiments (ultrasonic and low frequencies) on a tight carbonate sample and proposed a newly formulated squirt-flow model to describe the measurements. Their results indicate that there is not only a microscopic squirt-flow mechanism, but also other dispersion mechanisms. Li et al. (2020) analyzed the influence of different water saturations on the dispersion and attenuation of tight carbonate rocks within the seismic band (1–1000 Hz). It is shown that wave propagation theory, which considers only a single set of wave-induced fluid flow, is not sufficient to explain the observed dispersion phenomenon in the seismic frequency range. Rashid et al. (2022) measured porosities, permeabilities, and electrical conductivities of carbonates to infer the relationships between the diagenetic processes, the accompanying microstructural changes of the rock, and the physical properties of the rock. Zhao et al. (2023) carried out elastic wave velocity measurements on ultra-deep carbonate reservoir samples. Their results highlight the dominant influence of cracks and fluid types on the elastic responses of ultra-deep carbonates.

Geng et al. (2023) developed a high-temperature and high-pressure ultrasonic measurement system for rock and measured the ultrasonic wave velocities of nine ultra-deep carbonate samples. It was found that the effect of temperature on the elastic properties is greater than that of the confining pressure.

It is evident that the pores and cracks of rocks affects the elastic and electrical properties, and this effect has been studied using the effective medium model (e.g., Benveniste, 1987; Bruggeman, 1935; Carcione et al., 2003; Eshelby, 1957; Kuster and Toksöz, 1974; Mori and Tanaka, 1973; Seleznev et al., 2006; Walsh, 1965). Considering that pores and cracks with different aspect ratios can close or expand with increasing or decreasing pressure, the experimental data at different pressures can be used to estimate the pore geometry (Cheng and Toksöz, 1979; Deng et al., 2015; David and Zimmerman, 2012; Wang and Tang, 2021; Zhang et al., 2019). However, most models are mainly used to simulate a single physical rock property, which leads to ambiguous estimation of pore geometry. The joint inversion of multiple physical rock properties, such as elastic and electrical properties, can be helpful to improve the reliability of pore geometry estimation (e.g., Aquino-López et al., 2015; Han, 2018; Han et al., 2016; Watanabe et al., 2019; Zhang et al., 2022b). Akamatsu et al. (2023) measured the electrical resistivity and P- and S-wave velocities of oceanic crustal rocks under dry and saturated conditions. They combined the effective medium model of Kachanov (1994) (Kachanov model) with the statistical crack flow model of Guéguen and Dienes (1989) and analyzed the effects of microstructural crack parameters on the elastic and electrical properties.

The studies on the measurement of elastic and electrical properties of tight carbonates are still scarce, and the relevant characteristics and relationships need to be explored. We select two tight-carbonate samples dominated by cracks. We measure porosity, electrical conductivity and ultrasonic velocities under different effective pressures (the difference between the confining and pore pressures) and in a brine-saturated condition. In addition, the ultrasonic velocities of nitrogen-saturated samples are measured. The Kachanov model, which was originally applicable to cracked media, is then extended to a scenario with multiple cracks. It is combined with a multiphase REDEM model to simulate the elastic and electrical properties, inverting the crack aspect ratio spectra. Since both models are based on the same crack parameters, we investigate the rationality of predicting one physical property from another given the same crack geometry. Similar so-called cross-property relations have been proposed by Carcione et al. (2007).

2. Rock samples, experimental setup and results

2.1. Samples

The two tight carbonate samples (TC1 and TC2) come from the Metajan district (Yu et al., 2014). They are cylindrical cut with 37.89/38.10 mm diameter and 50.06/41.20 mm length. As shown in Fig. 1, both samples have intergranular dissolution pores filled with calcite after diagenetic alteration. The predominant pore space consists of cracks. X-ray diffraction analysis shows that the mineral composition of the samples is mainly calcite, with minor amounts of quartz and clay (Table 1).

2.2. Experimental procedure

The experimental setup used in the study is shown in Fig. 2 and consists of pore-pressure, confining-pressure and temperature control units, and ultrasonic-wave, electrical-resistance and fluid control units. The experimental procedure is as follows. (1) For nitrogen saturation experiments, the samples are first dried in an
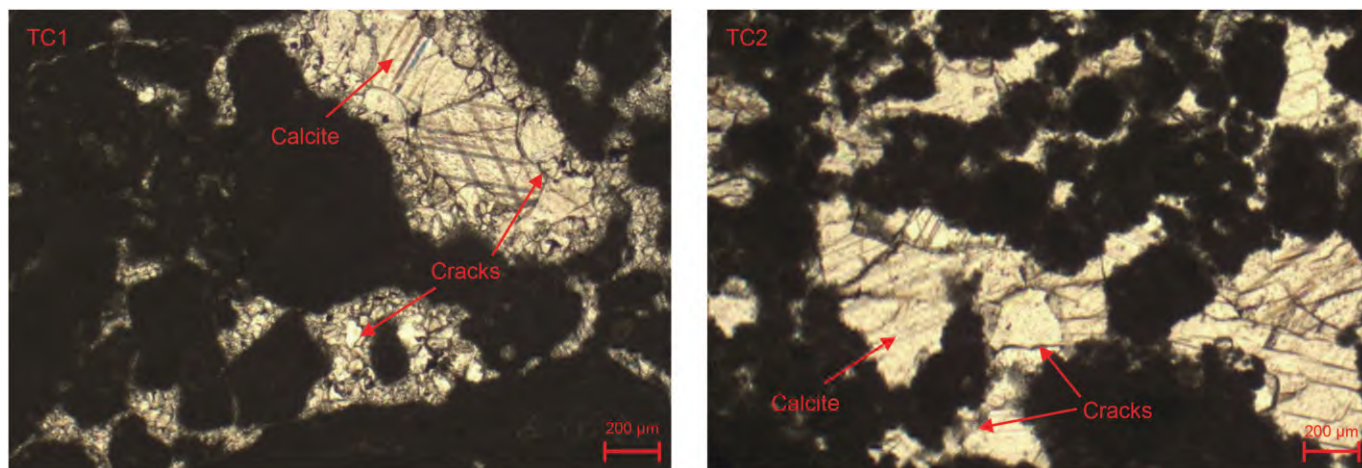
Fig. 1. Thin sections of samples TC1 and TC2.

Table 1
Properties of the samples.

Sample	TC1	TC2
Porosity, %	0.66	1.16
Dry density, kg/m³	2674	2661
Quartz, %	0.71	0.50
Calcite, %	98.69	98.48
Clay, %	0.60	1.02

oven. After cooling, they are placed in a sealed core holder where nitrogen gas is introduced through the fluid control unit and the pore pressure is maintained at 10 MPa with a confining pressure of 15 MPa. While keeping the pore pressure at the same value, the confining pressure is increased from 15 MPa to 100 MPa. After reaching each pressure point, the pressure is maintained for 2 h and the ultrasonic wave velocities are determined using the pulse transmission method. The measured frequencies of the P and S waves are 1 MPa and 0.5 MHz, respectively. (2) For the saturation

Fig. 2. A schematic diagram showing the joint elastic-electrical measurement system.

experiments with brine, the samples are saturated using a saturation procedure similar to Ba et al. (2023). Using the same procedure as in step (1), the ultrasonic velocities of the samples saturated with brine are measured. In addition, the electrical resistance of the samples is measured using an impedance-capacitance-resistance meter. The porosity of the samples is determined based on the initial porosity and the volume of liquid displaced from the core after pressurization. The bulk modulus and density of nitrogen/brine used in the experiments are 0.0161/2.25 GPa and 112.6/1000 kg/m³, respectively. The electrical conductivity of the brine is 5.56 S/m.

2.3. Results

2.3.1. Porosity and conductivity

Fig. 3 shows the porosity and electrical conductivity as a function of effective pressure for TC1 and TC2 saturated with brine. It can be observed that both properties decrease non-linearly with increasing pressure. This behavior is attributed to the progressive closure of cracks with smaller aspect ratios as the pressure increases (Guéguen and Boutéca, 2004; Walsh, 1965). It is also noted that the decrease in conductivity as a function of pressure is more pronounced than that of porosity (the decrease in conductivity is 42.03% and 51.12% for TC1 and TC2, respectively, while the decrease in porosity is 27.77% and 29.09%, respectively), suggesting that cracks serve as the main pathways for fluid migration.

2.3.2. Ultrasonic velocities

Fig. 4 shows the P- and S-wave velocities as a function of the effective pressure for the two samples in nitrogen gas and brine saturated states. The results show a non-linear increase in ultrasonic velocities with increasing pressure for the two cases, with crack closure identified as the most important factor for this phenomenon. For the nitrogen gas saturated case, the increase in P(S) wave velocity is 10.93% (8.18%) and 12.64% (10.49%) for the two samples. In the saturated brine case, the increase in P(S) wave velocity is 3.71% (4.76%) and 3.67% (5.80%). This behavior suggests that the brine, with its higher elastic modulus, may hinder the closure of cracks under loading.

Fig. 5 shows the corresponding V_P/V_S evolution with the effective pressure for samples TC1 and TC2. The values are in the range of 1.84—1.98 and 1.82—1.90 for the two cases. This is close to the values reported by Zhao et al. (2023) for tight carbonates (1.75—2.00). When the effective pressure is less than 50 MPa, the
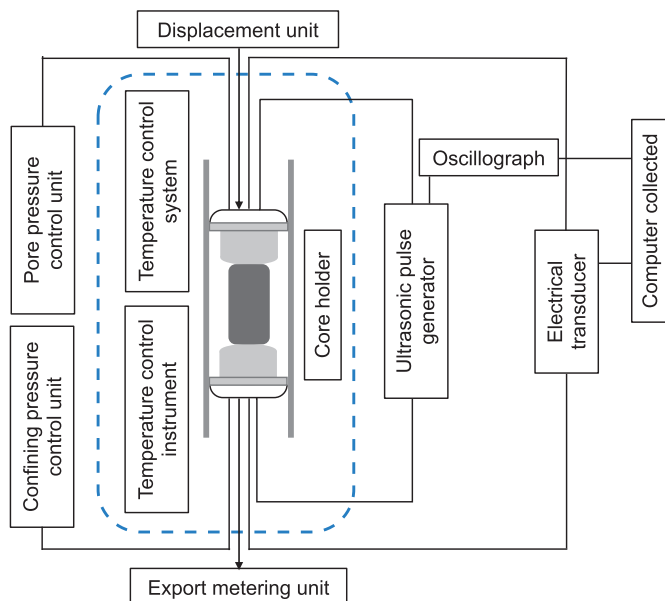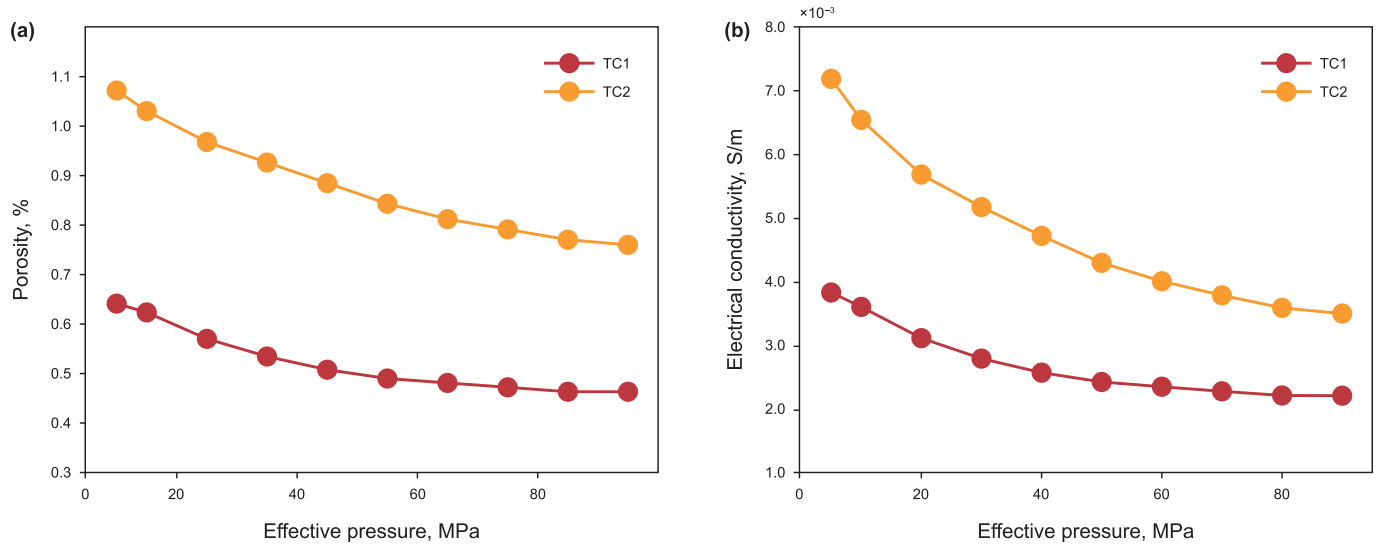
Fig. 3. Porosity (**a**) and electrical conductivity (**b**) as a function of the effective pressure for samples TC1 and TC2 in the brine-saturated state.
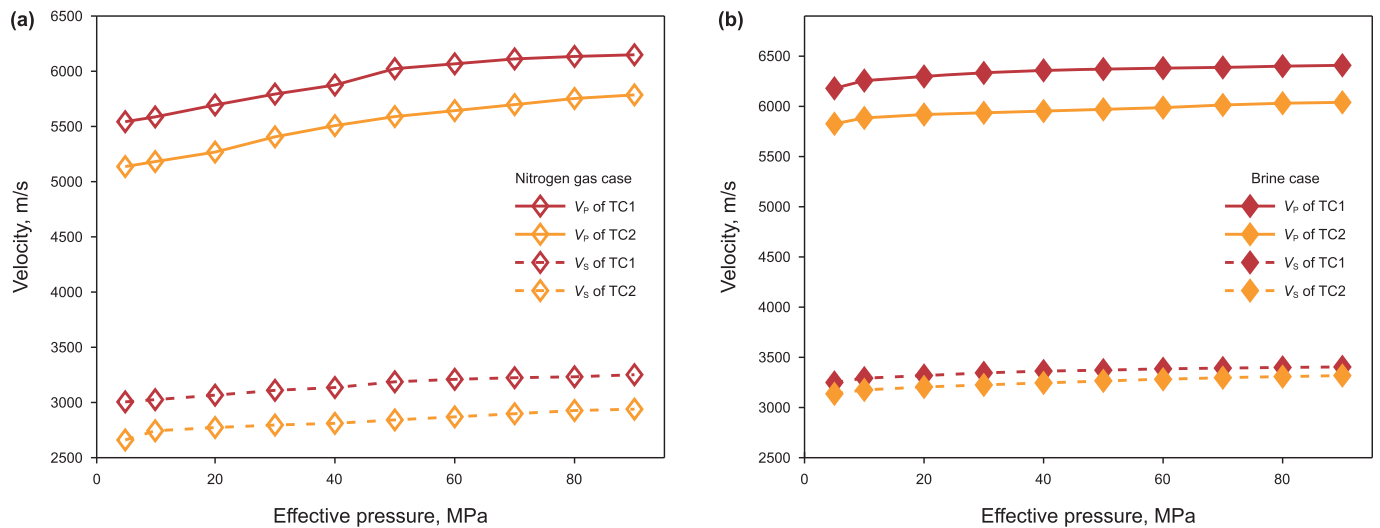

Fig. 4. P- and S-wave velocities as a function of the effective pressure for TC1 and TC2 in the nitrogen gas- (**a**) and brine-saturated (**b**) states.

value of nitrogen-saturated samples increases sharply with increasing pressure, while the value of brine-saturated samples decreases. However, when the effective pressure is in the range of 50−90 MPa, the values tend to be nearly constant. Similar experimental observations were made in Fortin et al. (2007) and Wang et al. (2012).

3. Theoretical models

3.1. Multiphase Kachanov model

By considering that the pore space of samples TC1 and TC2 consists mainly of cracks, the model of Kachanov (1993), which is based on the non-interaction approximation, can be used to simulate the measurements. The model assumes that the medium consists of penny-shaped cracks with identical aspect ratio, which are randomly distributed, and the effective elastic moduli (K^* and G^*) are expressed as follows:

$$\frac{K_0}{K^*} = 1 + \frac{h\rho_c}{1-2\nu_0}\left(1 - \left[1 - \left(1-\frac{\nu_0}{2}\right)\frac{\delta_c}{1+\delta_c}\right]\right), \tag{1}$$

$$\frac{G_0}{G^*} = 1 + \frac{h\rho_c}{1+\nu_0}\left(1 - \frac{2}{5}\left[1 - \left(1-\frac{\nu_0}{2}\right)\frac{\delta_c}{1+\delta_c}\right]\right), \tag{2}$$

where K_0 (G_0) is the bulk (shear) modulus of the matrix in the absence of cracks, and ν_0 is the corresponding Poisson ratio. h is the geometrical factor of penny-shaped cracks, δ_c is the dimensionless parameter for penny-shaped cracks, and the expressions of h and δ_c can be found in Appendix A. Crack density ρ_c is given by

$$\rho_c = \frac{\varphi_c}{2\pi\alpha}, \tag{3}$$

where φ_c is the crack porosity.

Assuming that a real rock consists of cracks with different aspect ratio α_k ($k = 1, 2, \cdots, K$) and there are interactions between neighboring cracks, the Kachanov model is extended to multiple cracks
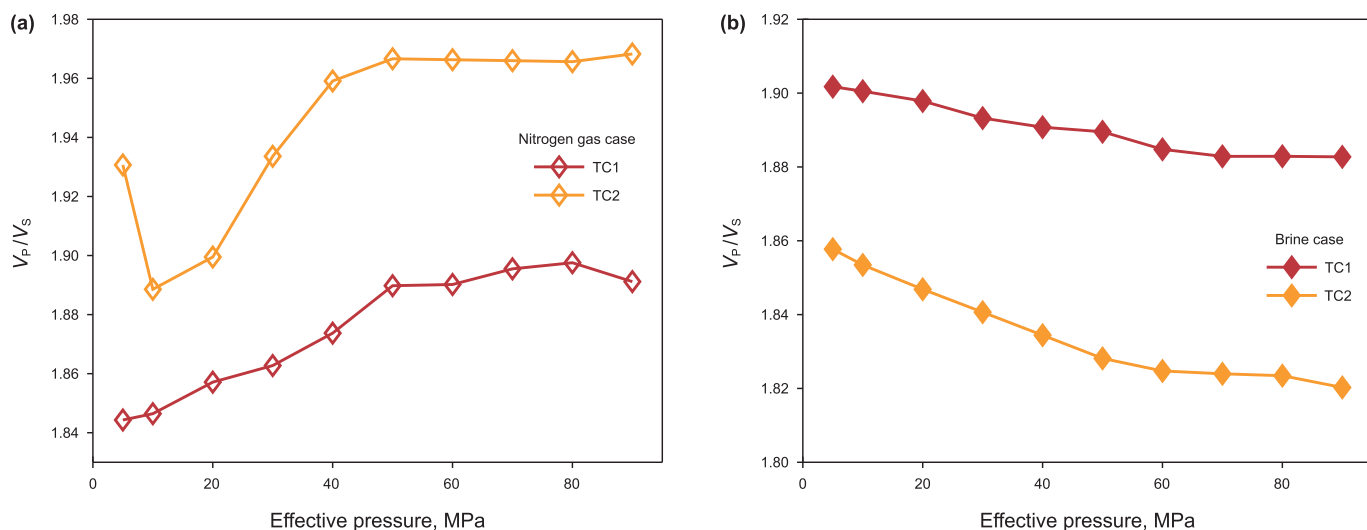
4013

Fig. 5. V_P/V_S as a function of the effective pressure for TC1 and TC2 in the nitrogen gas- (**a**) and brine-saturated (**b**) states.

(multiphase Kachanov model) by using the incremental algorithm developed by Berg (2007). After following each addition of cracks in the modeling process, a new cracked medium is established, which serves as a host/background phase for subsequent additions. Using Eqs. (1)−(3) in each addition, we stop the additions until all cracks are added. The modeling details of pressure-dependent elastic
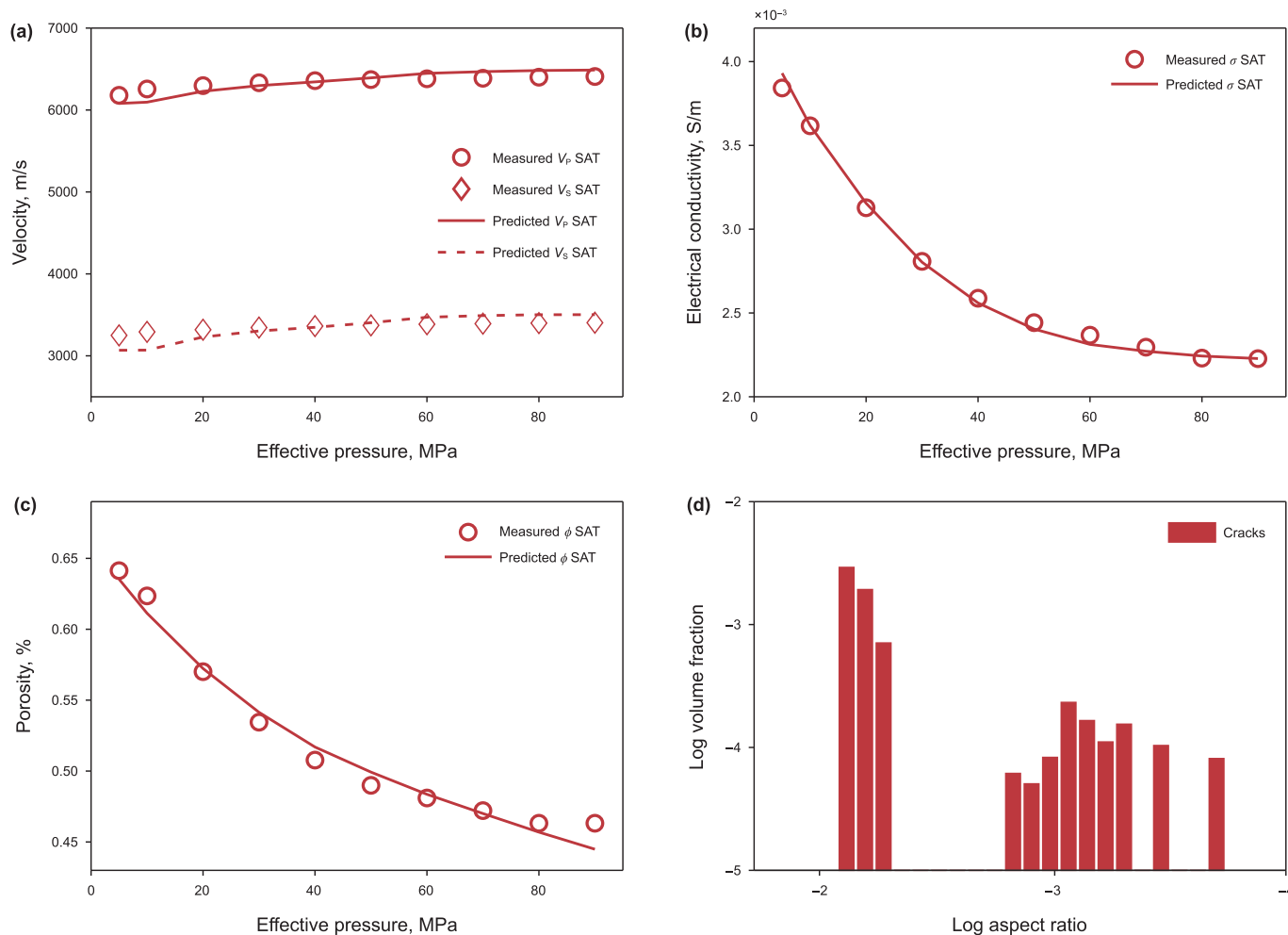

Fig. 6. Joint elastic-electrical inversion for sample TC1. (**a**) P- and S-wave velocities, (**b**) electrical conductivity, (**c**) porosity, where the symbols refer to the experimental data and the solid/dashed lines to the theory; (**d**) the inverted crack aspect ratio spectrum at zero effective pressure. SAT represents the brine saturated case.
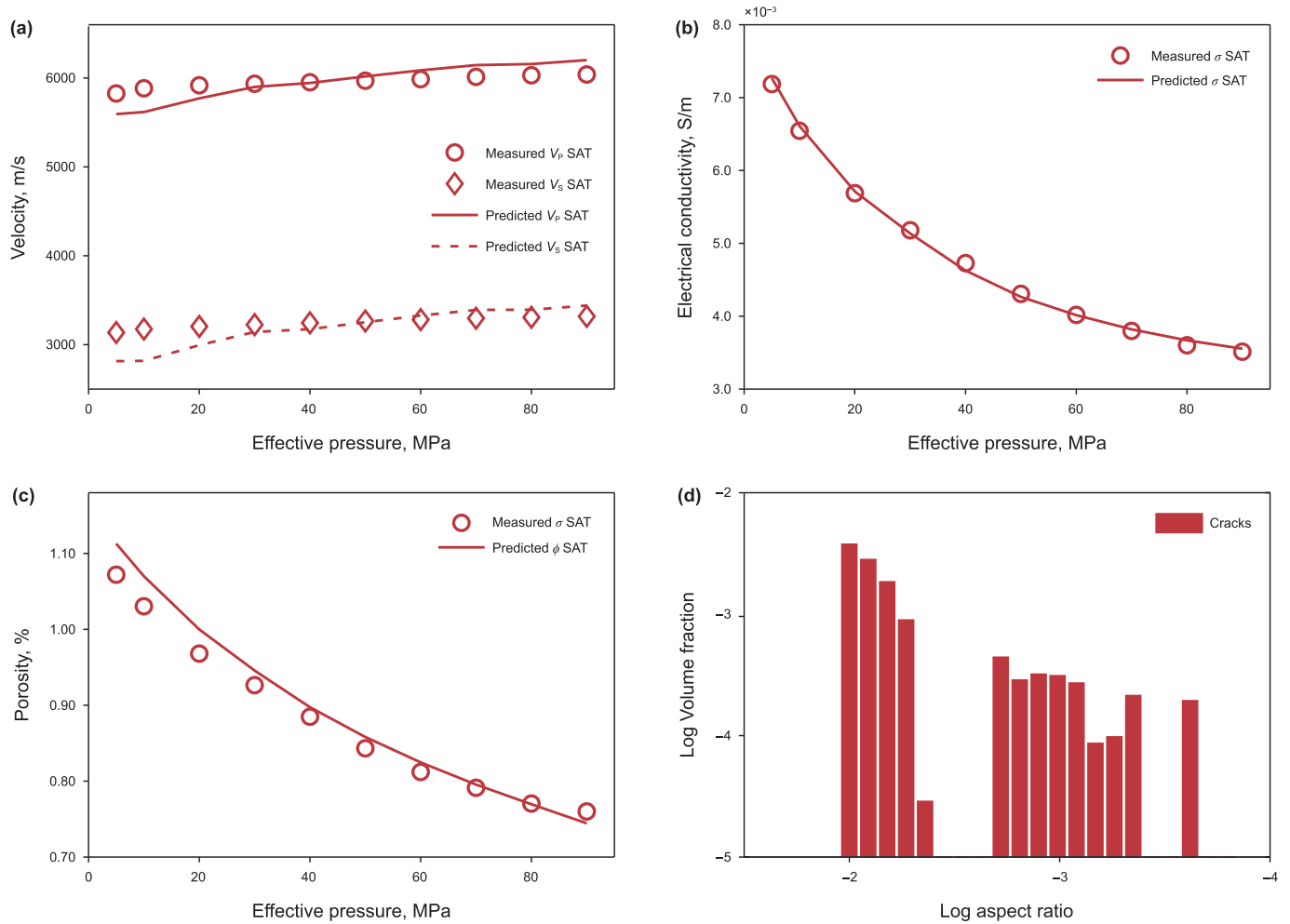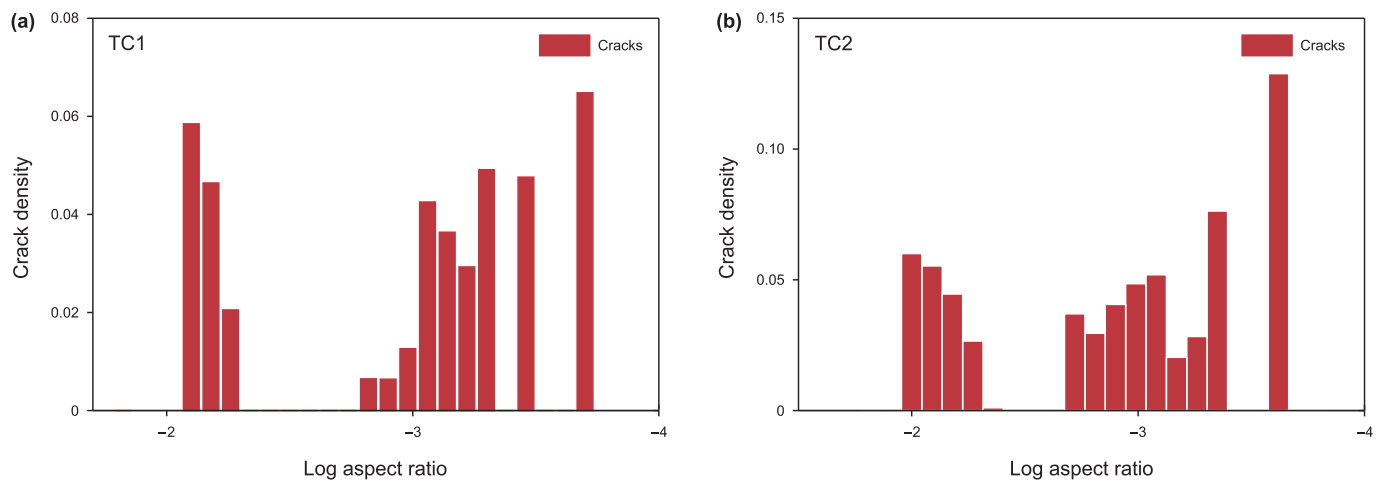
Fig. 7. Same as Fig. 6 for sample TC2.

Fig. 8. Corresponding crack densities for samples TC1 (**a**) and TC2 (**b**) at zero effective pressure.

properties are given in Appendix B.

3.2. Multiphase REDEM model

In the classical electrical DEM model, the fluid is usually considered as the host/background phase and solid particles are gradually added as inclusions to simulate the electrical properties. The order of addition of inclusions differs from that of the elastic DEM model, resulting in different distribution characteristics of pore geometry within the same rock. To ensure the consistency of
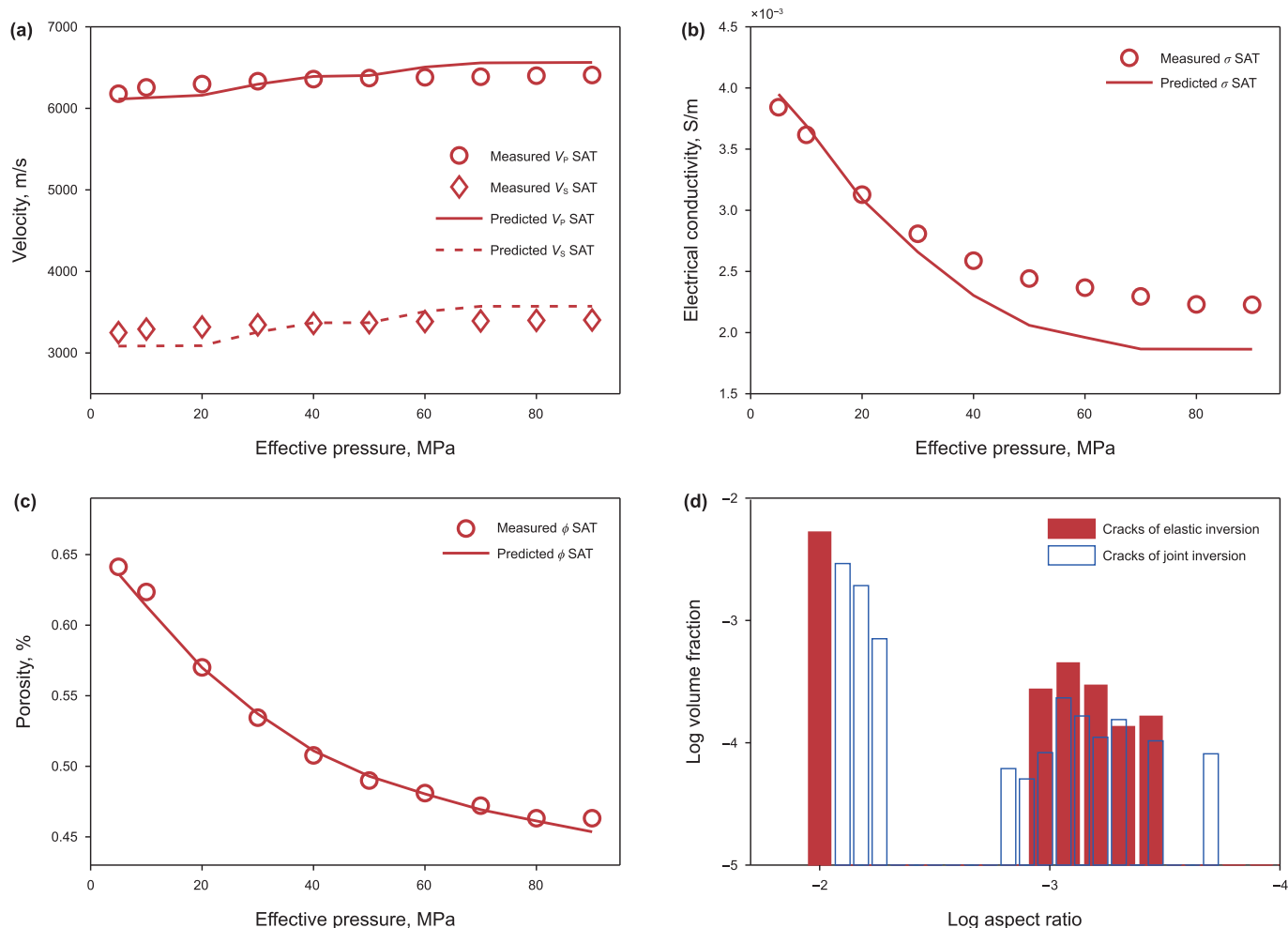
Fig. 9. Elastic inversion for sample TC1. **(a)** P- and S-wave velocities, **(b)** electrical conductivity, **(c)** porosity, where the symbols refer to the experimental data and the solid/dashed lines to the theory; **(d)** inverted crack aspect ratio spectrum at zero effective pressure.

the inclusion order with the elastic DEM model, Cilli and Chapman (2021) redeveloped the electrical DEM model (REDEM) for a two-phase medium and defined the relationship between the electrical properties of cracked media and the crack geometry as follows:

$$\frac{\mathrm{d}\sigma^*}{\mathrm{d}c} = 3\sigma^* \frac{(\sigma_i - \sigma^*)R^{(*i)}}{(1-c)}, \tag{4}$$

with $\sigma^*(c=0) = \sigma_0$, and σ_0, σ^* and σ_i are the grain, effective and inclusion electrical conductivities, respectively. The expression of parameter R is also given in Appendix A. Similarly, the REDEM model is extended to the case with multiple cracks by using the incremental algorithm, and the modeling details of pressure-dependent electrical properties are described in Appendix B.

3.3. Estimation of crack geometry

Based on the above model, the ultrasonic velocities and the electrical conductivity of rock are functions of the crack aspect ratio and the crack volume fraction (i.e., the crack aspect ratio spectrum). To estimate the spectrum, we perform a joint inversion of the measured velocities and conductivities using the models. In the inversion, the elastic moduli of the grains are treated as unknown parameters, since the use of mineral or average moduli from Voigt-Reuss-Hill averaging (Hill, 1952) is not possible (Qin et al., 2022). In addition, to improve the accuracy of the inversion results, the experimental porosities at different pressures are considered as constraints. The objective function (the mean square error between the theoretically predicted values and the measured values) can be expressed as follows:

$$F_{\mathrm{ela}}(\alpha_{01}, \alpha_{02}, \cdots \alpha_{0k}, c_{01}, c_{02}, \cdots c_{0k}, K_0, \mu_0, \sigma_0) = \min\left[\sum_{n=1}^{N}\left(V_{\mathrm{P},n}^{\mathrm{m}} - V_{\mathrm{P},n}^{\mathrm{p}}\right)^2 + \sum_{n=1}^{N}\left(V_{\mathrm{S},n}^{\mathrm{m}} - V_{\mathrm{S},n}^{\mathrm{p}}\right)^2 + \sum_{n=1}^{N}\left(\varphi_n^{\mathrm{m}} - \varphi_n^{\mathrm{p}}\right)^2 + \sum_{n=1}^{N}\left(\sigma_n^m - \sigma_n^{\mathrm{p}}\right)^2\right], \tag{5}$$
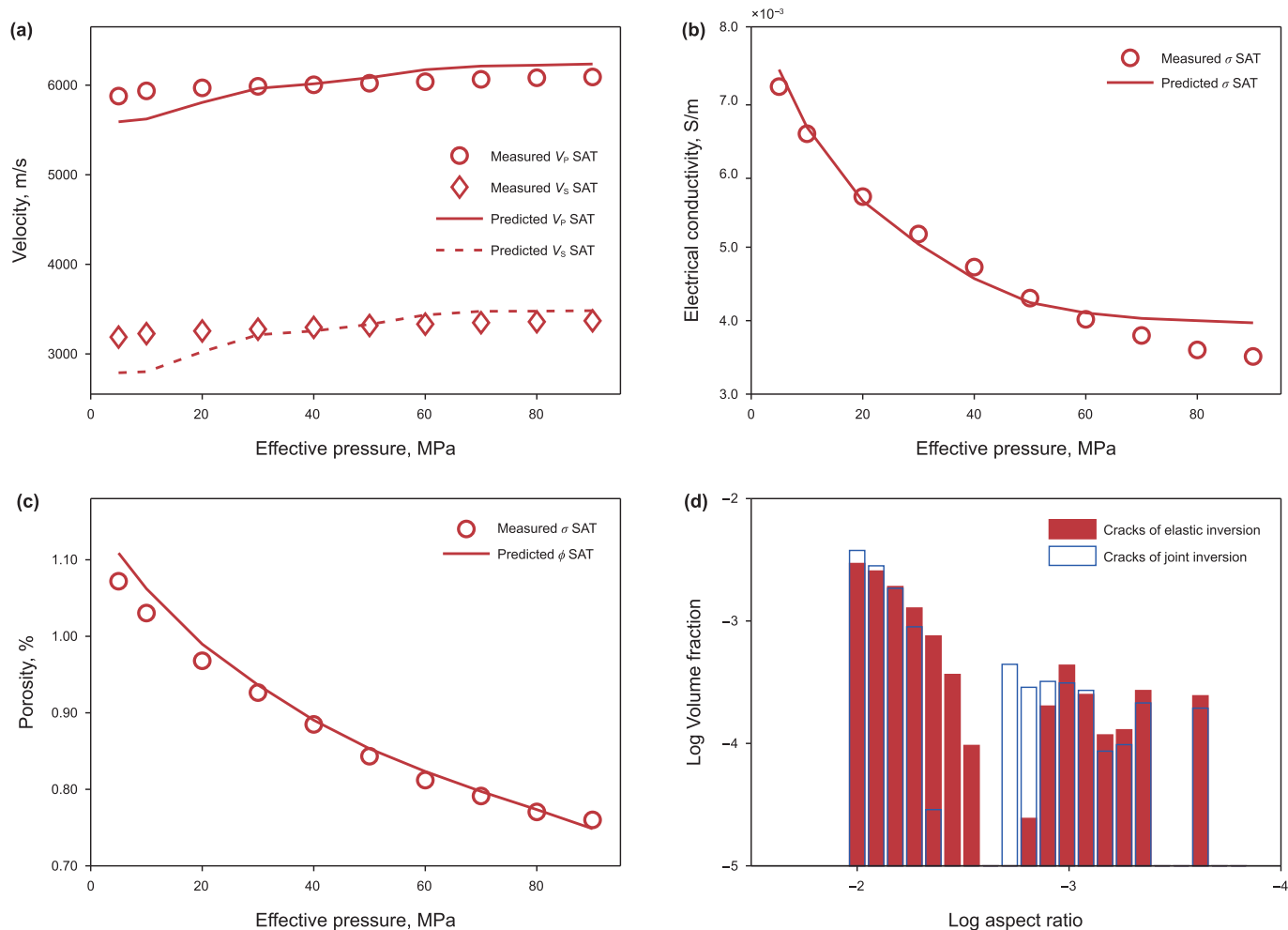
Fig. 10. Same as Fig. 9 for sample TC2.

where N is the number of pressure points, $V_{P,n}^{m}$, $V_{S,n}^{m}$, φ_{n}^{m} and σ_{n}^{m} are the experimental P- and S-wave velocities, porosity and electrical conductivity at the n-th effective pressure $P_{e,n}$, respectively, and $V_{P,n}^{p}$, $V_{S,n}^{p}$, φ_{n}^{p} and σ_{n}^{p} are the predictions. In the inversion, the distribution range of crack aspect ratio is set to 10^{-5} to 10^{-2}, with equal log-normal spacing based on the previous study (Zhang et al., 2022b). The simulated annealing method (e.g., Ingber, 1993) is used to minimize Eq. (5).

4. Inversion of crack geometry

4.1. Crack geometry by the joint elastic-electrical inversion

The joint elastic-electrical inversion results of TC1 and TC2 are shown in Figs. 6 and 7. The inverted bulk and shear moduli of the grains are 79/74.21 GPa and 37.5/40 GPa, respectively. Although the content of calcite in the two samples is more than 98%, there are discrepancies between the inverted values and the properties of calcite (76.8/32 GPa according to Mavko et al. (2009)). This finding provides the supporting evidence for the potential influence of factors such as grain sorting and shape, cement, pore fillings, and crystal defects on the grain moduli, as were proposed by Qin et al. (2022). The corresponding grain conductivities are 0.0012 S/m and 0.0014 S/m, respectively, which are higher than those of calcite (1.74E−04 S/m according to Saeed et al. (2022)). Figs. 6(a) and 7(a)

show a comparison between the experimental and predicted velocities under the different effective pressures for the brine-saturated case. The results indicate a good agreement between the predicted velocities and the experimental data at high effective pressures. However, the predicted values at low effective pressures are slightly lower than the corresponding experimental results. Figs. 6(b), 6(c), 7(b) and 7(c) show that the predictions are in good agreement with the experimental data. The inverted crack aspect ratio spectra at zero effective pressure are shown in Figs. 6(d) and 7(d), revealing a range of aspect ratios between 0.0002 and 0.0079 for TC1 and 0.00024 and 0.01 for TC2.

The crack density of samples TC1 and TC2 at zero effective pressure can be determined using Eq. (B-4), as shown in Fig. 8. The crack densities range from 0.0002 to 0.0079 and from 0.00024 to 0.01, and the overall crack densities are 0.43 and 0.65 for samples TC1 and TC2, respectively. It can be seen that the crack densities of the different crack types are all below the threshold value for the percolation of a cracked medium of about 0.13. This threshold represents the minimum crack density required to create a complete path for fluid flow (Guéguen and Dienes, 1989; Sarout et al., 2017). Consequently, the permeability of the two samples cannot be measured during the experiment. It is noted that the crack density corresponding to the crack type with the smallest aspect ratio in TC2 is much higher than that of the other cracks, indicating that the cracks tend to be closed with increasing pressure, resulting in a significant increase in ultrasonic wave velocities at low
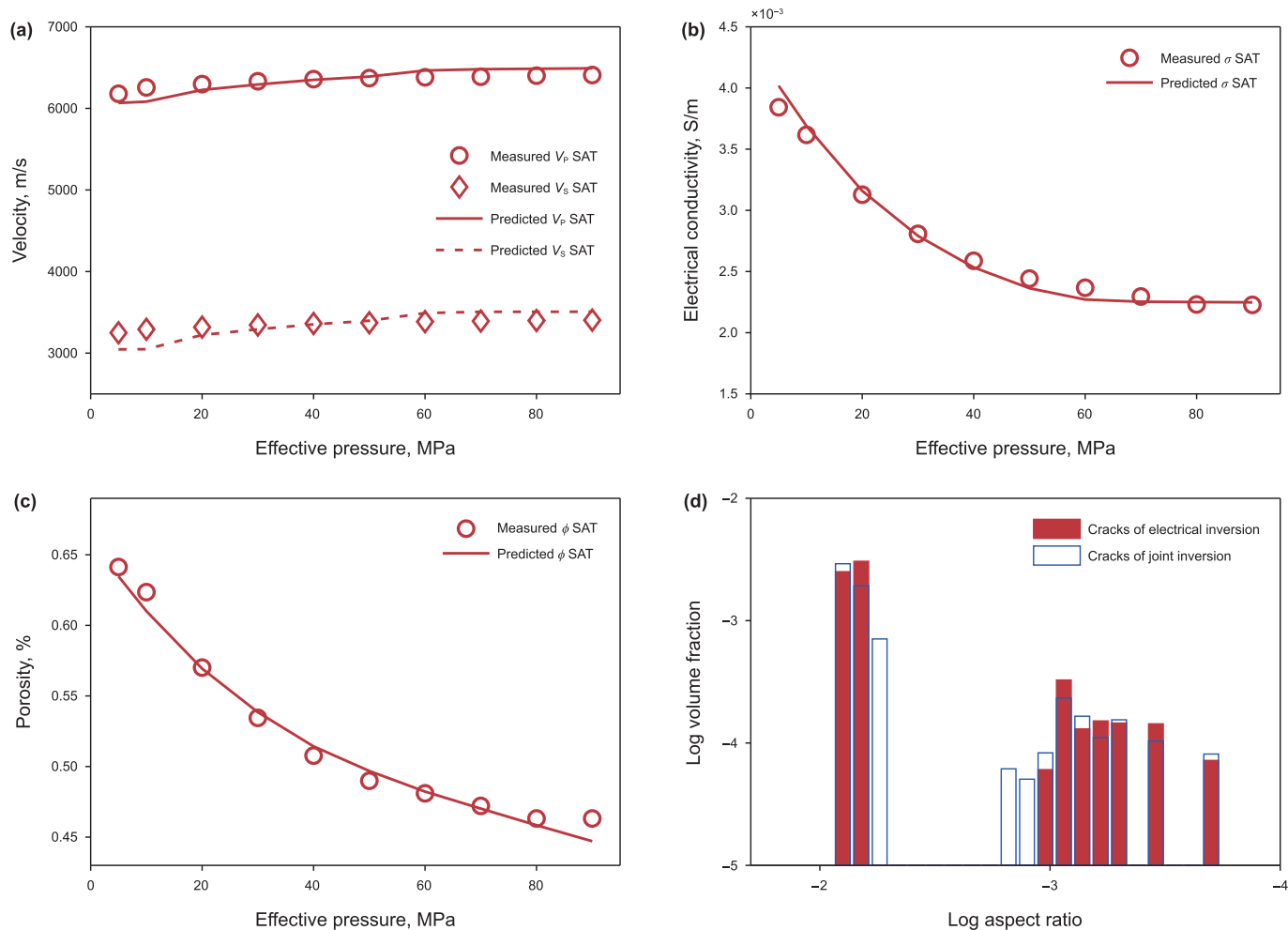
Fig. 11. Same as Fig. 9 for the electrical inversion (sample TC1).

effective pressures, and there is a significant decrease in conductivity and porosity.

4.2. Crack geometry from the elastic/electrical inversion

To further verify the results of the joint inversion, we perform comparisons with crack geometries obtained separately from the elastic or electric inversion. The grain properties used in these inversions are consistent with the values presented in Section 4.1. Figs. 9 and 10 show the results of the elastic inversion for samples TC1 and TC2, respectively. It can be observed that the predicted velocities and porosity agree well with the experimental data (Fig. 9(a) and 9(c) as well as Fig. 10(a) and 10(c)). The crack spectra obtained from the elastic inversions are shown in Figs. 9(d) and 10(d) and range from 0.00036 to 0.01 and 0.00024 to 0.01, respectively. These results serve as input to the multiphase REDEM model to estimate the conductivity. Figs. 9(b) and 10(b) show that the predictions for both samples agree very well with the experimental data in the low effective pressure range, while they deviate from the data in the high effective pressure range.

The electrical inversion for samples TC1 and TC2 is shown in Figs. 11 and 12, respectively. It can be seen that the predicted conductivity and porosity agree well with the experimental data (Fig. 11(b) and 11(c) as well as Fig. 12(b) and 12(c)). The crack aspect ratio spectra obtained from the electrical inversions are shown in Figs. 11(d) and 12(d), with both spectra showing a consistent

distribution range of 0.0002−0.0079. These results are also fed into the multiphase Kachanov model to predict the velocities. Figs. 11(a) and 12(a) show that the predicted velocities agree well with the experimental data, with the exception that the predicted value of TC2 at an effective pressure of 5 MPa is smaller than the measurement. Comparisons of Figs. 6(d) and 7(d) show that there are differences between the crack aspect ratio spectra from the elastic and electrical inversion and the result of the joint inversion, indicating that although the prediction of conductivity (ultrasonic velocities) using the aspect ratio spectrum inverted from the ultrasonic velocities (conductivity) appears to be optimal, the predicted crack geometry may not fully reflect the actual spatial distribution of cracks in the rock.

5. Discussion

5.1. Assessment of the experimental data

In some of the joint elastic-electrical studies (Akamatsu et al., 2023; Han et al., 2016; Zhang et al., 2022b), the ultrasonic velocities, electrical conductivity and porosity used were mainly measured by the different experimental setups. This method may result in cracks with lower aspect ratio closing in the initial tests that do not reopen in the subsequent tests, indicating that the crack geometry within the same rock becomes inconsistent during the tests. In addition, the different measurement methods can lead to
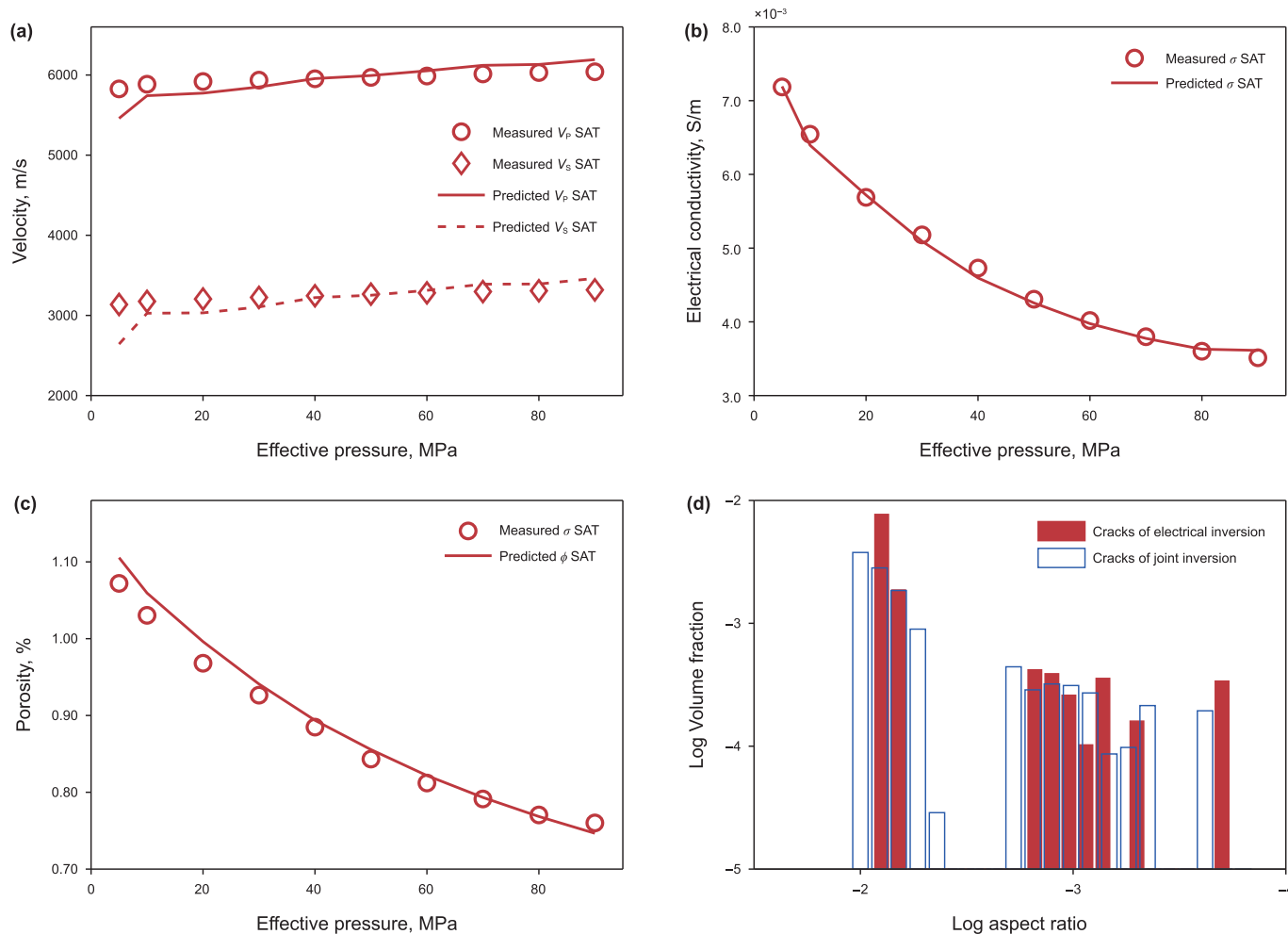
Fig. 12. Same as Fig. 11 for sample TC2.

different measurement results. Subsequently, the porosities of the two samples are determined by the helium expansion method (referred to as gas porosity) and the water saturation method

Fig. 13. Gas porosity and water porosity of samples TC1 and TC2.

(referred to as water porosity). The corresponding experimental results are shown in Fig. 13. The water porosity is larger than the gas porosity, and the largest differences between gas and water porosity in TS1 and TS2 are 0.211% and 0.362%, respectively. This is because the pore pressure in the water saturation method test (i.e., 10 MPa) is higher than that in the helium expansion method test (i.e., 2 MPa), which causes some cracks to remain open in the first test, while they are gradually closed in the second test. Another reason is that the physical properties of water and helium are quite different and the paths of fluid flow through a rock can be different, which can lead to the differences in the measured physical properties. This point was confirmed by the work of Pimienta et al. (2015), who measured the permeability of Fontainebleau sandstone using water and glycerol as pore fluids and found that the results obtained were different. This difference leads to a large error between the predicted crack geometry and that of the real rock, suggesting that it is essential to use the same device for the simultaneous measurement of the different physical properties of the rock. This can help to eliminate or reduce the influence of changes in test conditions on the crack geometry and ensures the consistency of the inverted crack geometry based on the measurements (Benson et al., 2006).
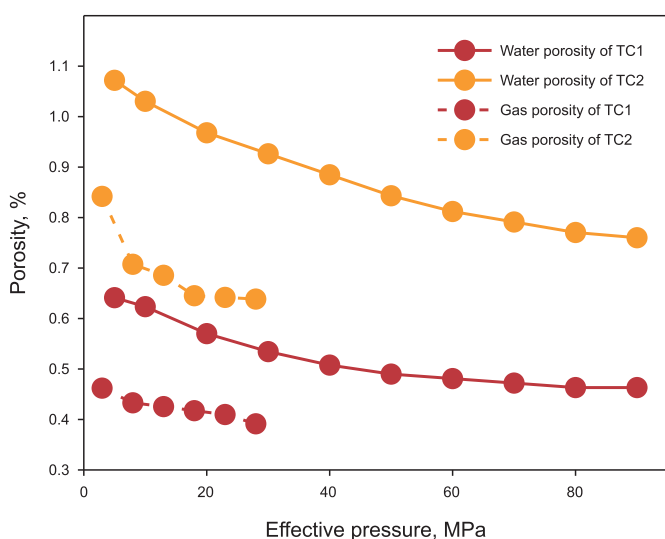
5.2. Comparison with the Kachanov model

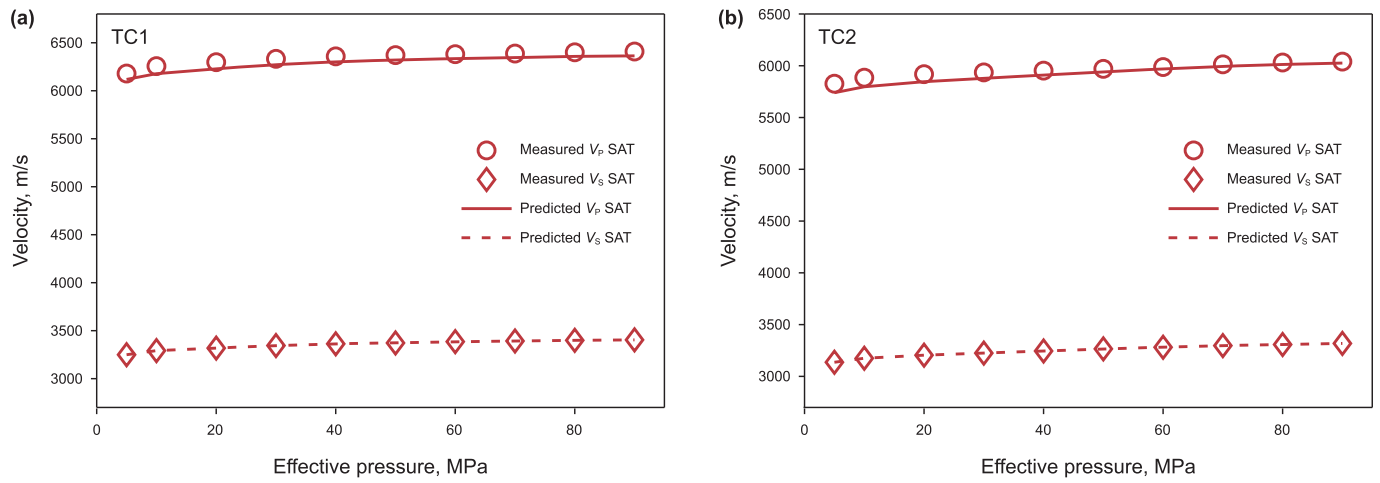Based on the inverse grain properties in Section 4.1, the

Fig. 14. Experimental data and predictions of the P- and S-wave velocities from the Kachanov model for the brine-saturated samples TC1 (**a**) and TC2 (**b**).
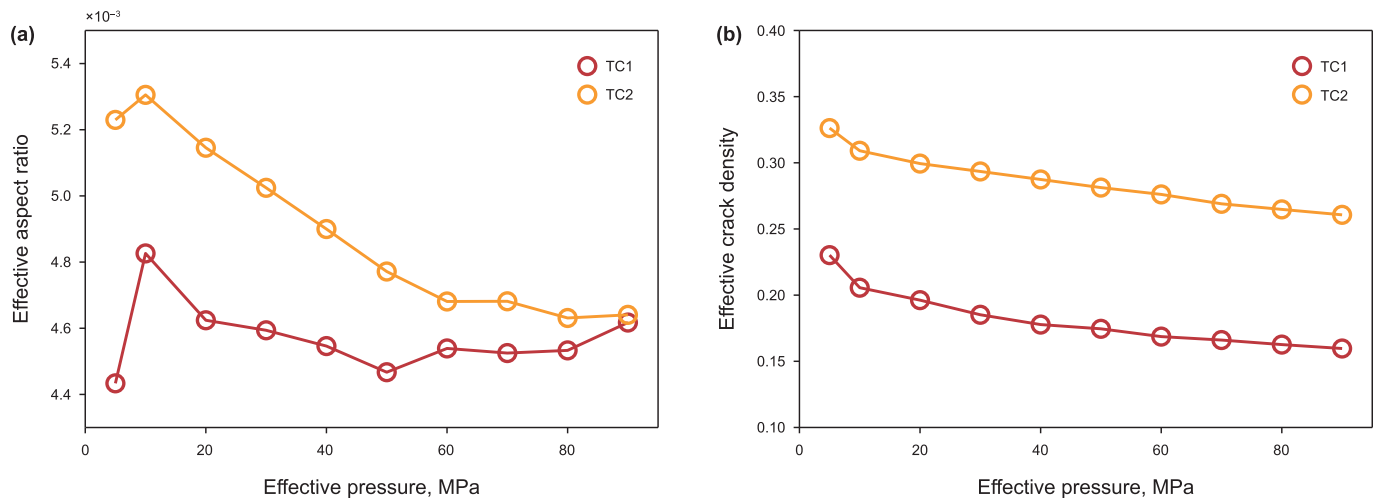

Fig. 15. Inverted effective crack aspect ratios and crack densities for samples TC1 (**a**) and TC2 (**b**).

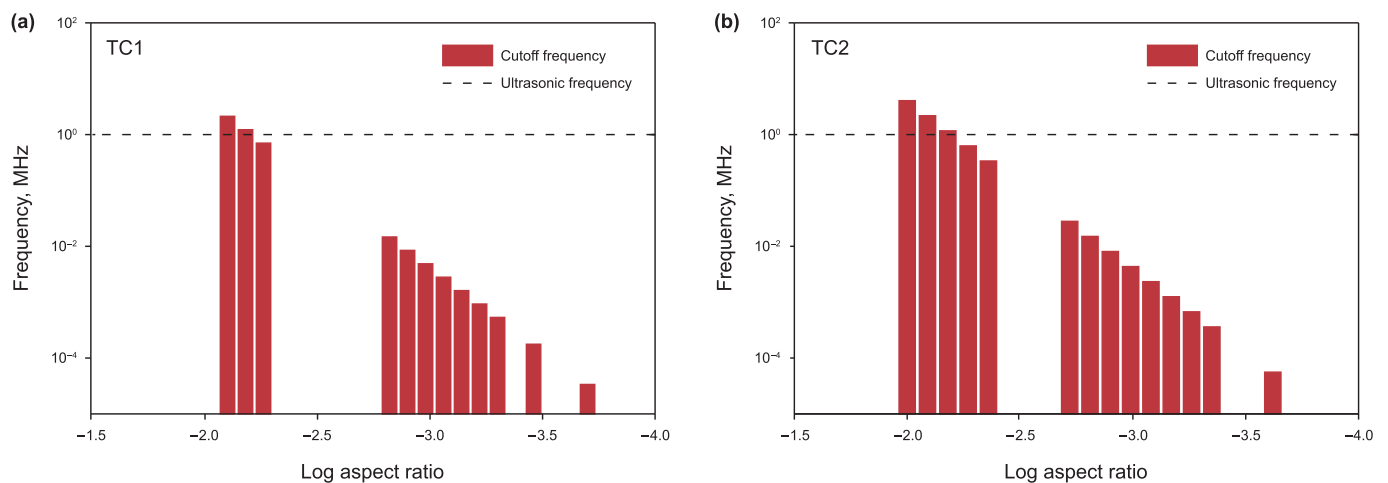**Fig. 16.** Squirt-flow cutoff frequencies corresponding to each crack in samples TC1 (**a**) and TC2 (**b**) at zero effective pressure.

Kachanov model is used to simulate the ultrasonic velocities, and the simulation results are shown in Fig. 14. It can be seen that the

velocities of brine-saturated samples predicted by the Kachanov model are almost consistent with the experimental data, and the

predicted results are much better than the results of the elastic or joint inversions. Assuming that the Kachanov model characterizes the influence of the actual crack geometry on the elastic properties of the rock in a similar way as an equivalent population of identical cracks with the same aspect ratio (referred to as "effective crack"), the effective crack aspect ratio and crack density of samples TC1 and TC2 at different effective pressures are obtained (Fig. 15). Fig. 15(a) shows that at an effective pressure of less than 15 MPa, the effective crack aspect ratio of the two specimens increases with increasing pressure. This result is consistent with the conclusions of Sarout et al. (2017). They suggested that the phenomenon is attributed to the first contact of opposing asperities in the rock in this pressure range. Specifically, the crack radius decreases while the crack opening remains largely unchanged, leading to an increase in the effective aspect ratio. As the pressure increases further, the crack aspect ratio decreases. This finding is consistent with the results of Sarout et al. (2017), where the reduction in the effective aspect ratio is attributed to the decreasing crack opening and increasing crack radius as the pressure increases.

Fig. 15(b) shows the effective crack densities of samples TC1 and TC2 in response to pressure. The crack density decreases with increasing pressure, which is consistent with the results of Benson et al. (2006) and Sarout et al. (2017). The crack density is attributed to the progressive closure of cracks at increased pressure. The effective crack density of the two samples is less than the total crack density obtained from the joint inversion, but greater than the percolation threshold ~0.13. This indicates that the crack network in the samples is interconnected and thus permeability is present, contradicting the experimental inability to measure permeability. The simplified representation of the complex crack geometry in a real rock as a group of cracks with the same aspect ratio and radius may not be realistic.

5.3. Validity of the model

According to Adelinet et al. (2011) and Sarout et al. (2017), the squirt flow cut-off frequency between adjacent microcracks is $f_{sq} \sim E_0\alpha^3/(24\eta)$ (E_0 is the Young modulus of the matrix with the absence of cracks, and η is the fluid viscosity), and the corresponding cut-off frequencies of the individual cracks in the two samples are shown in Fig. 16. Compared with the frequency of the P-wave measurement (1 MHz), it can be seen that the pore fluid flow (i.e., squirt flow) exists between cracks at low effective pressures (Dvorkin et al., 1995; Mavko and Jizba, 1991; Wu et al., 2020), or squirt flow occurs between the clay-related cracks (Ba et al., 2016). The described flow mechanisms contribute to the stiffening of the rock skeleton, but the proposed multiphase Kachanov model does not account for these mechanisms. This may be important for the predicted P-wave velocity in the low effective pressure region, which is slightly lower than the experimental result. For S-waves, pore fluid flow (shear strain hardening phenomenon) may also occur between some cracks under shear wave excitation (Shafiro and Kachanov, 1997). The proposed model did not take this effect into account either, which may also lead to the predicted S-wave velocity in the low effective pressure region being lower than the experimental result.

6. Conclusions

The P- and S-wave velocities and the electrical conductivity were measured for the two tight carbonate samples. The variations in velocities and conductivity as a function of pressure can be related to the closure or expansion of cracks in the rock. To analyze the effects of crack geometry on the elastic and electrical properties of the tight carbonates, a multiphase Kachanov model is proposed

and integrated with a multiphase reformulated electrical differential effective medium (REDEM) model to describe the measurements. The comparison between the theoretical predictions and the experimental data shows that the joint elastic and electrical inversion has a satisfactory performance. In a future study, the sample pool may be extended and more experimental data can be used to check the validity of model. Furthermore, the crack geometry from the joint inversion is estimated and compared with that from the separate elastic or electrical inversions. The results show that the crack geometries obtained from different physical properties are different, and the models provide a way to predict the change of one property of cracked rock from the measurement of another.

CRediT authorship contribution statement

Lin Zhang: Writing − original draft, Validation, Supervision, Software, Methodology, Investigation, Formal analysis, Conceptualization. **Li Gao:** Validation, Data curation, Investigation, Software, Formal analysis. **Jing Ba:** Writing − review & editing, Visualization, Funding acquisition, Investigation, Project administration, Supervision. **José M. Carcione:** Writing − review & editing, Formal analysis, Conceptualization, Investigation, Supervision, Validation. **Jin-Yi Min:** Visualization, Validation, Supervision, Software, Methodology, Investigation, Conceptualization.

Declaration of competing interest

The authors declare that they have no known competing financial interests or personal relationships that could have appeared to influence the work reported in this paper.

Acknowledgements

Appendix A. Expressions of *h* and *R*

The geometrical factor *h* of penny-shaped cracks is

$$h = \frac{16(1 - \nu_0^2)}{9(1 - \nu_0/2)}, \tag{A-1}$$

and the dimensionless parameter δ_c for penny-shaped cracks is

$$\delta_c = \frac{9\pi\alpha K_0(1 - 2\nu_0)}{16K_f(1 - \nu_0^2)}, \tag{A-2}$$

where K_f is the fluid bulk modulus, and α is the crack aspect ratio.
The parameter *R* is

$$R = \frac{1}{9}\sum_{j=a,b,c}\frac{1}{L_j\sigma_i + (1 - L_j)\sigma^*}, \tag{A-3}$$

where L_a, L_b and L_c are depolarization factors of penny-shaped ellipsoidal inclusions, and the subscripts a, b and c are the three major axes of these inclusions.

Appendix B. Modeling details of pressure-dependent physical properties

To model the pressure-dependence of elastic or electrical properties, the changes of volume fraction with respect to the effective pressure (P_e) are as follows,

$$\frac{dc}{c} = -\frac{P_e/K_d^*}{E_1 - \frac{E_2 E_3}{E_3 + E_4}}, \tag{B-1}$$

where $E_1 - E_4$ are functions of α and the effective static moduli of the rock with all the pores except those with the aspect ratio α, and K_d^* is the effective static bulk modulus of the dry rock. These quantities are commonly considered to be equivalent to the dynamic moduli of the dry rock (Cheng and Toksöz, 1979; Tang et al., 2021). Then the volume fraction of cracks at the n-th effective pressure $P_{e,n}$ is given by (Cheng, 1978),

$$c_{nk} = c_{0k}\left(1 + \frac{dc}{c}(\alpha_{0k}, P_{e,n})\right), \tag{B-2}$$

where c_{0k} and c_{nk} are volume fractions at zero effective pressure and $P_{e,n}$, respectively, and α_{0k} is the aspect ratio at zero effective pressure. By considering that the change of crack aspect ratio with pressure is the same as that for its volume fraction (Cheng and Toksöz, 1979), i.e., $d\alpha/\alpha = dc(\alpha)/c(\alpha)$, the aspect ratio of the cracks at $P_{e,n}$ is

$$\alpha_{nk} = \alpha_{0k}\left(1 + \frac{dc}{c}(\alpha_{0k}, P_{e,n})\right), \tag{B-3}$$

where α_{nk} is the aspect ratio at $P_{e,n}$. When $d\alpha/\alpha \leq -1$, the cracks are considered to be closed. By using Eq. (3), the crack density of the cracks at $P_{e,n}$ is

$$\rho_{nk} = \frac{c_{nk}}{2\pi\alpha_{nk}}. \tag{B-4}$$

References

Adam, L., Batzle, M., Brevik, I., 2006. Gassmann's fluid substitution and shear modulus variability in carbonates at laboratory seismic and ultrasonic frequencies. Geophysics 71 (6), F173–F183. https://doi.org/10.1190/1.2358494.

Adelinet, M., Fortin, J., Guéguen, Y., 2011. Dispersion of elastic moduli in a porous-cracked rock: theoretical predictions for squirt-flow. Tectonophysics 503 (1–2), 173–181. https://doi.org/10.1016/j.tecto.2010.10.012.

Akamatsu, Y., Nagase, K., Abe, N., et al., 2023. Cross-property relationship between electrical resistivity and elastic wave velocity of crustal rocks from the Oman drilling project hole Gt3a: implications for in situ geophysical properties of oceanic crust. J. Geophys. Res. Solid Earth, e2022JB026130. https://doi.org/10.1029/2022JB026130.

Anselmetti, F.S., Eberli, G.P., 1993. Controls on sonic velocity in carbonates. Pure Appl. Geophys. 141, 287–323. https://doi.org/10.1007/BF00998333.

Anselmetti, F.S., Von Salis, G.A., Cunningham, K.J., et al., 1997. Acoustic properties of Neogene carbonates and siliciclastics from the subsurface of the Florida Keys: implications for seismic reflectivity. Mar. Geol. 144 (1–3), 9–31. https://doi.org/10.1016/S0025-3227(97)00081-9.

Aquino-López, A., Mousatov, A., Markov, M., et al., 2015. Modeling and inversion of elastic wave velocities and electrical conductivity in clastic formations with structural and dispersed shales. J. Appl. Geophys. 116, 28–42. https://doi.org/10.1016/j.jappgeo.2015.02.013.

Ara, T.S., Talabani, S., Vaziri, H.H., et al., 2001. In-depth investigation of the validity of the Archie equation in carbonate rocks. In: SPE Production and Operations Symposium. https://doi.org/10.2118/67204-MS.

Archie, G.E., 1942. The electrical resistivity log as an aid in determining some reservoir characteristics. Trans. AIME 146 (1), 54–62. https://doi.org/10.2118/942054-G.

Assefa, S., Mccann, C., Sothcott, J., 2003. Velocities of compressional and shear waves in limestones. Geophys. Prospect. 51 (1), 1–13. https://doi.org/10.1046/j.1365-2478.2003.00349.x.

Ba, J., Zhang, L., Wang, D., et al., 2018. Experimental analysis on P-wave attenuation in carbonate rocks and reservoir identification. J. Seismic Explor. 27 (4), 371–402.

Ba, J., Xu, W., Fu, L.Y., et al., 2017. Rock anelasticity due to patchy saturation and fabric heterogeneity: a double double-porosity model of wave propagation. J. Geophys. Res. Solid Earth 122 (3), 1949–1976. https://doi.org/10.1002/2016JB013882.

Ba, J., Zhao, J., Carcione, J.M., et al., 2016. Compressional wave dispersion due to rock matrix stiffening by clay squirt flow. Geophys. Res. Lett. 43 (12), 6186–6195. https://doi.org/10.1002/2016GL069312.

Ba, J., Zhu, H., Zhang, L., et al., 2023. Effect of multiscale cracks on seismic wave propagation in tight sandstones. J. Geophys. Res. Solid Earth 128 (10), e2023JB027474. https://doi.org/10.1029/2023JB027474.

Baechle, G.T., Weger, R.J., Eberli, G.P., et al., 2005. Changes of shear moduli in carbonate rocks: implications for Gassmann applicability. Lead. Edge 24 (5), 507–510. https://doi.org/10.1190/1.1926808.

Bakhorji, A., Schmitt, D., 2022. Understanding carbonates from Saudi Arabia: laboratory measurements of elastic properties: Part I. J. Appl. Geophys. 206, 104820. https://doi.org/10.1016/j.jappgeo.2022.104820.

Batzle, M.L., Han, D.H., Hofmann, R., 2006. Fluid mobility and frequency-dependent seismic velocity—direct measurements. Geophysics 71 (1), N1–N9. https://doi.org/10.1190/1.2159053.

Behin, R., 2004. Investigation on the effect of stress on cementation factor of Iranian carbonate oil reservoir rocks. In: International Symposium of the Society of Core Analysts Held in Abu Dhabi, UAE (SCA 2004-41).

Benson, P., Schubnel, A., Vinciguerra, S., et al., 2006. Modeling the permeability evolution of microcracked rocks from elastic wave velocity inversion at elevated isostatic pressure. J. Geophys. Res. Solid Earth 111 (B4). https://doi.org/10.1029/2005JB003710.

Benveniste, Y., 1987. A new approach to the application of Mori-Tanaka's theory in composite materials. Mech. Mater. 6 (2), 147–157. https://doi.org/10.1016/0167-6636(87)90005-6.

Berg, C., 2007. An effective medium algorithm for calculating water saturations at any salinity or frequency. Geophysics 72 (2), E59–E67. https://doi.org/10.1190/1.2432261.

Borai, A.M., 1987. A new correlation for the cementation factor in low-porosity carbonates. SPE Form. Eval. 2 (4), 495–499. https://doi.org/10.2118/14401-PA.

Borgomano, J.V.M., Pimienta, L, Fortin, J., et al., 2017. Dispersion and attenuation measurements of the elastic moduli of a dual-porosity limestone. J. Geophys. Res. Solid Earth 122 (4), 2690–2711. https://doi.org/10.1002/2016JB013816.

Borgomano, J.V., Pimienta, L.X., Fortin, J., et al., 2019. Seismic dispersion and attenuation in fluid-saturated carbonate rocks: effect of microstructure and pressure. J. Geophys. Res. Solid Earth 124 (12), 12498–12522. https://doi.org/10.1029/2019JB018434.

Brace, W.F., Orange, A.S., Madden, T.R., 1965. The effect of pressure on the electrical resistivity of water-saturated crystalline rocks. J. Geophys. Res. 70 (22), 5669–5678. https://doi.org/10.1029/JZ070i022p05669.

Bruggeman, V.D., 1935. Berechnung verschiedener physikalischer Konstanten von heterogenen Substanzen. I. Dielektrizitätskonstanten und Leitfähigkeiten der Mischkörper aus isotropen Substanzen. Ann. Phys. 416 (7), 636–664. https://doi.org/10.1002/andp.19354160705 (in German).

Carcione, J.M., Seriani, G., Gei, D., 2003. Acoustic and electromagnetic properties of soils saturated with salt water and NAPL. J. Appl. Geophys. 52, 177–191. https://doi.org/10.1016/S0926-9851(03)00012-0.

Carcione, J.M., Ursin, B., Nordskag, J.I., 2007. Cross-property relations between electrical conductivity and the seismic velocity of rocks. Geophysics 72, E193–E204. https://doi.org/10.1190/1.2762224.

Cheng, C.H., 1978. Seismic Velocities in Porous Rocks — Direct and Inverse Problems. Massachusetts Institute of Technology,. Sc.D. thesis.

Cheng, C.H., Toksöz, M.N., 1979. Inversion of seismic velocities for the pore aspect ratio spectrum of a rock. J. Geophys. Res. Solid Earth 84 (B13), 7533–7543. https://doi.org/10.1029/JB084iB13p07533.

Cilli, P.A., Chapman, M., 2021. Linking elastic and electrical properties of rocks using cross-property DEM. Geophys. J. Int. 225 (3), 1812–1823. https://doi.org/10.1093/gji/ggab046.

David, E.C., Zimmerman, R.W., 2012. Pore structure model for elastic wave velocities in fluid-saturated sandstones. J. Geophys. Res. 117 (B7). https://doi.org/10.1029/2012JB009195.

Deng, S.G., Fan, Y.R., Duan, Z.F., et al., 2000. Experiment study of rock resistivity with multi-temperature and multi-salinity. Oil Geophys. Prospect. 35 (6), 763–767. https://doi.org/10.13810/j.cnki.issn.1000-7210.2000.06.011 (in Chinese).

Deng, J.X., Zhou, H., Wang, H., et al., 2015. The influence of pore structure in reservoir sandstone on dispersion properties of elastic waves. Chin. J. Geophys. 58 (9), 3389–3400. https://doi.org/10.6038/cjg20150931 (in Chinese).

Dvorkin, J., Mavko, G., Nur, A., 1995. Squirt flow in fully saturated rocks. Geophysics 60 (1), 97–107. https://doi.org/10.1190/1.1443767.

Eberli, G.P., Baechle, G.T., Anselmetti, F.S., et al., 2003. Factors controlling elastic properties in carbonate sediments and rocks. Lead. Edge 22 (7), 654–660. https://doi.org/10.1190/1.1599691.

El-Husseiny, A., Vanorio, T., 2015. The effect of micrite content on the acoustic velocity of carbonate rocks. Geophysics 80 (4), L45–L55. https://doi.org/10.1190/geo2014-0599.1.

Eshelby, J.D., 1957. The determination of the elastic field of an ellipsoidal inclusion, and related problems. Proc. Roy. Soc. Lond. Math. Phys. Sci. 241 (1226), 376–396. https://doi.org/10.1098/rspa.1957.0133.

Fortin, J., Guéguen, Y., Schubnel, A., 2007. Effects of pore collapse and grain crushing on ultrasonic velocities and Vp/Vs. J. Geophys. Res. Solid Earth 112 (B8). https://doi.org/10.1029/2005JB004005.

Geng, J., Zhao, L., Ma, J., et al., 2023. High-temperature and high-pressure ultrasonic experimental studies on elastic properties of ultra-deep carbonate reservoir rocks. Chin. J. Geophys. 66 (9), 3959–3974. https://doi.org/10.6038/cjg2023Q0374 (in Chinese).

Guéguen, Y., Boutéca, M., 2004. Mechanics of Fluid-saturated Rocks. Academic Press, New York.

Guéguen, Y., Dienes, J., 1989. Transport properties of rocks from statistics and percolation. Math. Geol. 21 (1), 1–13. https://doi.org/10.1007/BF00897237.

Guo, J., Gurevich, B., 2020. Frequency-dependent P wave anisotropy due to wave-induced fluid flow and elastic scattering in a fluid-saturated porous medium with aligned fractures. J. Geophys. Res. Solid Earth 125 (8), e2020JB020320. https://doi.org/10.1029/2020JB020320.

Guo, Y.Q., Ma, H.D., Shi, K.B., et al., 2013. Porous-grain-upper-boundary model and its application to Tarim Basin carbonates. Appl. Geophys. 10 (4), 411–422. https://doi.org/10.1007/s11770-013-0399-8.

Han, T., 2018. Joint elastic-electrical properties of artificial porous sandstone with aligned fractures. Geophys. Res. Lett. 45 (7), 3051–3058. https://doi.org/10.1002/2018GL077541.

Han, T., Clennell, M.B., Cheng, A.C., et al., 2016. Are self-consistent models capable of jointly modeling elastic velocity and electrical conductivity of reservoir sandstones? Geophysics 81 (4), D377–D382. https://doi.org/10.1190/geo2015-0690.1.

Hill, R., 1952. The elastic behaviour of a crystalline aggregate. Proc. Phys. Soc. 65 (5), 349. https://doi.org/10.1088/0370-1298/65/5/307.

Ingber, L., 1993. Simulated annealing: Practice versus theory. Math. Comput. Model. 18 (11), 29–57. https://doi.org/10.1016/0895-7177(93)90204-C.

Jia, C.Z., 2020. Development challenges and future scientific and technological researches in China's petroleum industry upstream. Acta Pet. Sin. 41 (12), 1445. https://doi.org/10.7623/syxb202012001 (in Chinese).

Kachanov, M., 1994. Elastic solids with many cracks and related problems. In: Hutchinson, J.W., Wu, T.Y. (Eds.), Adv Appl Mech, vol. 30. Elsevier, pp. 259–445. https://doi.org/10.1016/S0065-2156(08)70176-5.

Kachanov, M., 1993. Elastic solids with many cracks and related problems. Adv. Appl. Mech. 30, 259–445. https://doi.org/10.1016/S0065-2156(08)70176-5.

Kim, D.C., Manghnani, M.H., 1992. Influence of diagenesis on the electrical resistivity and the formation factor of deep-sea carbonate sediments. Geo Mar. Lett. 12, 14–18. https://doi.org/10.1007/BF02092103.

Kumar, M., Han, D.H., 2005. Pore shape effect on elastic properties of carbonate rocks. In: SEG International Exposition and Annual Meeting, SEG-2005. https://doi.org/10.1190/1.2147969.

Kuster, G.T., Toksöz, M.N., 1974. Velocity and attenuation of seismic waves in two-phase media: Part I. Theoretical formulations. Geophysics 39 (5), 587–606. https://doi.org/10.1190/1.1440450.

Li, Y., Shi, G., 2002. Experimental study on the relations between rock resistivity and temperature in simulating in-situ conditions. Acta Sci. Nauralium Univ. Pekin. 38 (6), 796–800 (in Chinese).

Li, C., Zhao, J., Wang, H., et al., 2020. Multi-frequency rock physics measurements and dispersion analysis on tight carbonate rocks. Chin. J. Geophys. 63 (2), 627–637. https://doi.org/10.6038/cjg2019M0294 (in Chinese).

Liu, S.G., Shan, Y.M., Huang, S.J., 2006. Characteristics and variation pattern of acoustic parameters of carbonate reservoir rocks in Tahe oil field Tarim basin. Oil Gas Geol. 27 (3), 399–404. https://doi.org/10.11743/ogg20060316 (in Chinese).

Mavko, G., Jizba, D., 1991. Estimating grain-scale fluid effects on velocity dispersion in rocks. Geophysics 56 (12), 1940–1949. https://doi.org/10.1190/1.1443005.

Mavko, G., Mukerji, T., Dvorkin, J., 2009. The Rock Physics Handbook Tools for Seismic Analysis of Porous Media, second ed. Cambridge University Press, New York.

Mori, T., Tanaka, K., 1973. Average stress in matrix and average elastic energy of materials with misfitting inclusions. Acta Metall. 21 (5), 571–574. https://doi.org/10.1016/0001-6160(73)90064-3.

Nourani, M., Pruno, S., Ghasemi, M., et al., 2023. Analytical models for predicting the formation resistivity factor and resistivity index at overburden conditions. Petrophys. SPWLA J. Form. Eval. Reserv. Descrip. 64 (3), 353–366. https://doi.org/10.30632/PJV64N3-2023a3.

Pan, J.G., Wang, H.B., Li, C., et al., 2015. Effect of pore structure on seismic rock-physics characteristics of dense carbonates. Appl. Geophys. 12 (1), 1–10. https://doi.org/10.1007/s11770-014-0477-1.

Pimienta, L., Fortin, J., Guéguen, Y., 2015. Experimental study of Young's modulus dispersion and attenuation in fully saturated sandstones. Geophysics 80 (5), L57–L72. https://doi.org/10.1190/geo2014-0532.1.

Qin, X., Han, D.-H., Zhao, L., 2022. Measurement of grain bulk modulus on sandstone samples from the Norwegian Continental Shelf. J. Geophys. Res. Solid Earth 127, e2022JB024550. https://doi.org/10.1029/2022JB0245.

Rashid, F., Hussein, D., Glover, P.W.J., et al., 2022. Quantitative diagenesis: methods for studying the evolution of the physical properties of tight carbonate reservoir rocks. Mar. Petrol. Geol. 139, 105603. https://doi.org/10.1016/j.marpetgeo.2022.105603.

Regnet, J.B., Robion, P., David, C., et al., 2015. Acoustic and reservoir properties of microporous carbonate rocks: implication of micrite particle size and morphology. J. Geophys. Res. Solid Earth 120 (2), 790–811. https://doi.org/10.1002/2014JB011313.

Ruan, C., Li, F., Ba, J., et al., 2023. Effects of temperature and pressure on the wave responses of deep carbonate reservoirs. J. Geophys. Eng. 20 (3), 610–620. https://doi.org/10.1093/jge/gxad033.

Saeed, A., Adewuyi, S.O., Ahmed, H.A., et al., 2022. Electrical and dielectric properties of the natural calcite and quartz. Silicon-Neth 14 (10), 5265–5276. https://doi.org/10.1007/s12633-021-01318-7.

Sarout, J., Cazes, E., Delle Piane, C., et al., 2017. Stress-dependent permeability and wave dispersion in tight cracked rocks: experimental validation of simple effective medium models. J. Geophys. Res. Solid Earth 122 (8), 6180–6201. https://doi.org/10.1002/2017JB014147.

Sayers, C.M., 2008. The elastic properties of carbonates. Lead. Edge 27 (8), 1020–1024. https://doi.org/10.1190/1.2967555.

Seleznev, N., Habashy, T., Boyd, A., Hizem, M., 2006. Formation properties derived from a multi-frequency dielectric measurement. In: SPWLA 47th Annual Logging Symposium. SPWLA, pp. 1–12.

Shafiro, B., Kachanov, M., 1997. Materials with fluid-filled pores of various shapes: effective elastic properties and fluid pressure polarization. Int. J. Solid Struct. 34 (27), 3517–3540. https://doi.org/10.1016/S0020-7683(96)00185-0.

Tang, X., Wang, H., Su, Y., et al., 2021. Inversion for micro-pore structure distribution characteristics using cracked porous medium elastic wave theory. Chin. J. Geophys. 64 (8), 2941–2951. https://doi.org/10.6038/cjg2021O0478 (in Chinese).

Tariq, Z., Mahmoud, M., Al-Youssef, H., et al., 2020. Carbonate rocks resistivity determination using dual and triple porosity conductivity models. Petroleum 6 (1), 35–42. https://doi.org/10.1016/j.petlm.2019.04.005.

Teillet, T., Fournier, F., Zhao, L., et al., 2021. Geophysical pore type inversion in carbonate reservoir: integration of cores, well logs, and seismic data (Yadana field, offshore Myanmar). Geophysics 86 (3), B149–B164. https://doi.org/10.1190/geo2020-0486.1.

Tian, H., Shen, A., Zhang, J., et al., 2019. New calculation method of cementation exponent m for crack-vuggy carbonate reservoirs. Chin. J. Geophys. 62 (6), 2276–2285. https://doi.org/10.6038/cjg2019L0633 (in Chinese).

Tian, H., Wang, G., Wang, K., et al., 2020. Study on the effect of pore structure on resistivity of carbonate reservoirs. Chin. J. Geophys. 63 (11), 4232–4243. https://doi.org/10.6038/cjg202O0110 (in Chinese).

Towle, G., 1962. An analysis of the formation resistivity factor-porosity relationship of some assumed pore geometries. In: SPWLA Annual Logging Symposium, SPWLA-1962.

Walsh, J.B., 1965. The effect of cracks on the compressibility of rock. J. Geophys. Res. 70 (2), 381–389. https://doi.org/10.1029/JZ070i002p00381.

Wang, X.Q., Schubnel, A., Fortin, J., et al., 2012. High Vp/Vs ratio: saturated cracks or anisotropy effects? Geophys. Res. Lett. 39 (11). https://doi.org/10.1029/2012GL051742.

Wang, H.M., Tang, X.M., 2021. Inversion of dry and saturated P-and S-wave velocities for the pore-aspect-ratio spectrum using a cracked porous medium elastic wave theory. Geophysics 86 (6), A57–A62. https://doi.org/10.1190/geo2021-0071.1.

Watanabe, T., Makimura, M., Kaiwa, Y., et al., 2019. Elastic wave velocity and electrical conductivity in a brine-saturated rock and microstructure of pores. Earth Planets Space 71 (1), 1–12. https://doi.org/10.1186/s40623-019-1112-9.

Wei, Y., Ba, J., Carcione, J.M., 2022. Stress effects on wave velocities of rocks: contribution of crack closure, squirt flow and acoustoelasticity. J. Geophys. Res. Solid Earth 127 (10), e2022JB025253. https://doi.org/10.1029/2022JB025253.

Wei, Y., Ba, J., Carcione, J.M., et al., 2021. Temperature, differential pressure, and porosity inversion for ultradeep carbonate reservoirs based on 3D rock-physics templates. Geophysics 86 (3), M77–M89. https://doi.org/10.1190/geo2020-0550.1.

Wei, W., Cai, J., Hu, X., et al., 2015. An electrical conductivity model for fractal porous media. Geophys. Res. Lett. 42 (12), 4833–4840. https://doi.org/10.1002/2015GL064460.

Wu, C., Ba, J., Carcione, J.M., et al., 2020. A squirt-flow theory to model wave anelasticity in rocks containing compliant microfractures. Phys. Earth Planet. In. 301, 106450. https://doi.org/10.1016/j.pepi.2020.106450.

Yu, H., Ba, J., Carcione, J., et al., 2014. Rock physics modeling of heterogeneous carbonate reservoirs: porosity estimation and hydrocarbon detection. Appl. Geophys. 11, 9–22. https://doi.org/10.1007/s11770-014-0413-9.

Yue, W., 2019. Pore-scale explanation of the Archie's cementation exponent: microstructure, electrical anisotropy, and numerical experiments. Geophys. Res. Lett. 46 (11), 5799–5807. https://doi.org/10.1029/2019GL082585.

Zhang, L., Ba, J., Carcione, J.M., 2021. Wave propagation in infinituple-porosity media. J. Geophys. Res. Solid Earth 126 (4), e2020JB021266. https://doi.org/10.1029/2020JB021266.

Zhang, L., Ba, J., Carcione, J.M., et al., 2022a. Seismic wave propagation in partially saturated rocks with a fractal distribution of fluid-patch size. J. Geophys. Res. Solid Earth 127 (2), e2021JB023809. https://doi.org/10.1029/2021JB023809.

Zhang, L., Ba, J., Fu, L., et al., 2019. Estimation of pore microstructure by using the static and dynamic moduli. Int. J. Rock Mech. Min. 113, 24–30. https://doi.org/10.1016/j.ijrmms.2018.11.005.

Zhang, L., Ba, J., Li, C., et al., 2022b. Joint inversion of the unified pore geometry of

tight sandstones based on elastic and electrical properties. J. Petrol. Sci. Eng. 219, 111109. https://doi.org/10.1016/j.petrol.2022.111109.

Zhao, L.X., Chen, M.J., 2015. A discussion on the relationships between five properties in reservoir evaluation. Nat. Gas. Ind. 35 (1), 53–60. https://doi.org/10.1016/j.ngib.2015.07.002.

Zhao, L., Ma, J., Li, K., et al., 2023. Seismic rock physics characteristics and modeling of ultra-deep carbonate reservoirs. Chin. J. Geophys. 66 (1), 16–33. https://doi.org/10.6038/cjg2022Q0382 (in Chinese).

Zhu, L., Wu, S., Zhang, C., et al., 2023. Characterization of pore electrical conductivity in porous media by weakly conductive and nonconductive pores. Surv. Geophys. 44 (3), 877–923. https://doi.org/10.1007/s10712-022-09761-w.